PCCP

Accepted Manuscript

ROYAL SOCIETY OF CHEMISTRY

www.rsc.org/pccp

PCCP

RSCPublishing

ARTICLE

Carrier dynamics of a visible-light-responsive Ta_3N_5 photoanode for water oxidation

Cite this: DOI: 10.1039/xoxxoooooox

Ahmed Ziani,[a] Ela Nurlaela,[a] Dattatray S. Dhawale,[a] Diego Alves Silva,[a] Erkki Alarousu,[b] Omar F. Mohammed,[b] and Kazuhiro Takanabe[a*]

Received ooth January 2012,
Accepted ooth January 2012

DOI: 10.1039/xoxxoooooox

www.rsc.org/

The physicochemical properties of a tantalum nitride (Ta_3N_5) photoanode were investigated in detail to understand fundamental aspects associated with the photoelectrochemical (PEC) water oxidation. The Ta_3N_5 thin films were synthesized using DC magnetron sputtering followed by annealing in air and nitridation under ammonia (NH_3). The polycrystalline structure with a dense morphology of the monoclinic Ta_3N_5 films was obtained. A relatively low absorption coefficient (10^4 to 10^5 cm^{-1}) in the visible light range was measured for Ta_3N_5, consistent with the nature of indirect band-gap. Ultra-fast spectroscopic measurements revealed that the Ta_3N_5 films possess low transport properties and have especially fast carrier recombination (< 10 ps) for the samples with various thickness. These critical kinetic properties of Ta_3N_5 as a photoanode may necessitate high overpotentials to achieve appreciable photocurrents for water oxidation (onset ~0.6 V vs. RHE).

Introduction

Considering the rarefaction of the current fossil energy resources and global warming worldwide, the question of finding a clean and cheap alternative to conventional energy has become an essential challenge for the scientific community. Recently, the production of hydrogen (H_2) by photoelectrochemical (PEC) water splitting under visible light irradiation is one of the most innovative solutions to tackle the above energy problems. [1-7] H_2 production from the naturally abundant both water and solar light sources can be achieved in the UV domain by broad band-gap-based oxide photocatalyst materials such as TiO_2,[8] or by photoactive oxides in the visible range (1.7-2.5 eV) such as hematite (α-Fe_2O_3), tungsten oxide (WO_3) or bismuth vanadate ($BiVO_4$).[9-12] These types of materials are only effective for half-reactions (oxidation) because of their insufficient reduction potential at bottom of the conduction band. For overall water splitting, the choice of photocatalysts is limited. The most promising photocatalysts are (oxy)nitride materials such as tantalum oxynitride (TaON), tantalum nitride (Ta_3N_5) or materials from the perovskite family.[13-18] Due to its good visible absorption (approximately 600 nm) and band positions that allow both water reduction and oxidation reactions, Ta_3N_5 has been extensively investigated for more than a decade as an attractive solar water splitting powder and photoanode.[19-23] Significantly high photocurrents for water oxidation, even at high applied potential (>0.6 V vs. RHE), have been reported when the photoanode is adequately modified with a cocatalyst such as CoPi[20-24] or a ferrihydrite complex as a hole scavenger,[11,22] achieving an applied bias photon-to-current efficiency ($ABPE_{AM1.5G}$) of 1.5%.[25] None of these works has discussed the optoelectronic and transport properties of Ta_3N_5, its intrinsic properties as a semiconductor, is essential to achieve the process.

In this study, our efforts are aimed at experimentally measuring absorption coefficient, carrier lifetime and charge carrier mobility of Ta_3N_5, by means of the ultra-fast transient absorption spectroscopy and the Hall effect measurements. To accurately measure these optical and spectroscopic properties, it was effective to have Ta_3N_5 in the form of crystalline thin films with flat surfaces. Therefore, a conventional sputtering method was intentionally used to obtain high-quality thin films. We do not intend to improve PEC performance but rather to gain an improved understanding of the intrinsic photophysical properties of Ta_3N_5 to identify the barrier that inhibits efficient PEC performance. The obtained Ta_3N_5 thin films were characterized to break down the complex PEC mechanism starting from the photon absorption to the charge carrier interaction with the electrolyte solution at the photocatalyst surface.

The majority of Ta_3N_5 thin films in the literature were obtained by post-calcination of Ta foil,[23,26-27] sputtering of Ta thin films,[27] or anodization of Ta.[20,24,28] One paper describes the direct sputtering of Ta_3N_5 by radio frequency (RF) sputtering with a mixture of $Ar/O_2/N_2$.[29] Herein, we report thin films with different thicknesses fabricated in a controlled manner using reactive direct current (DC) sputtering followed by annealing and nitridation to enhance the crystallinity. The various measurements including femtosecond (fs) transient absorption spectroscopy revealed a significant impact of the intrinsic lifetime of the excited carriers on the PEC performance of Ta_3N_5 films.

Results and discussion

Ta_3N_5 films were synthesized on tantalum (Ta) foil and fused glass substrates with different thickness from 50 to 470 nm by controlling the sputtering deposition time. In addition,

thicker samples with multiple sputtering intervals of Ta_3N_5 (3 × 320, and 6 × 160 nm) were fabricated (with 1 h intervals to avoid overheating of the Ta target), having average thicknesses estimated to be ~ 960 nm for both samples. All of the samples were annealed at 550 °C, followed by nitridation at 900 °C for 3 h. The crystal structures of the obtained films were characterized using XRD analysis, and the results are presented in Fig. 1a. Clearly, all of the films have a polycrystalline structure corresponding to the Ta_3N_5 monoclinic phase that is characterized by the presence of the five most intense peaks at 17.7º, 24.8º, 31.8º, 35.4º and 36.5º corresponding to the (200), (−202), (−203), (400) and (−113) planes, respectively. The crystallinity and grain size tends to increase with increasing thickness. The peaks become sharper and more intense with increasing thickness, especially for the *a*-axis orientation. One additional peak arising from the TaON impurity appeared at 29.5º for the thick films (470 nm and greater), which likely formed underneath the major Ta_3N_5 layer.

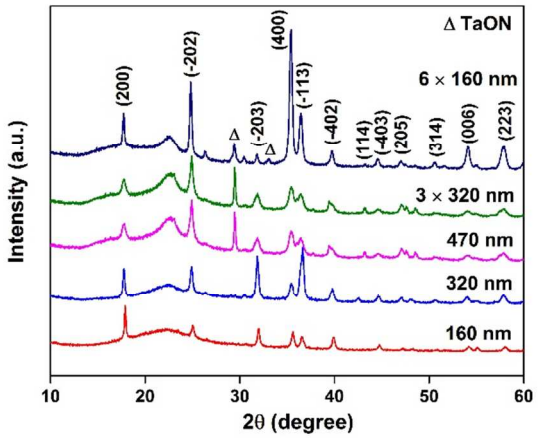

Fig. 1 The XRD patterns of Ta_3N_5 films at different thicknesses.

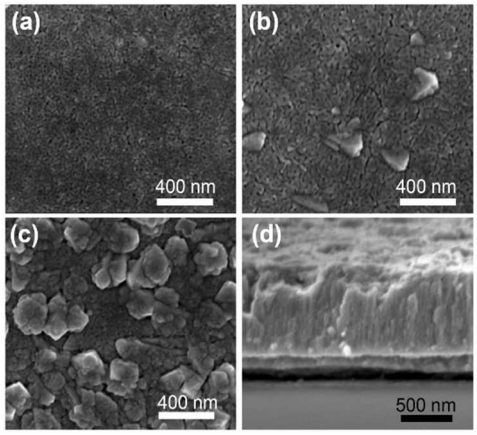

Fig. 2 The SEM images of Ta_3N_5 films at different thicknesses: (a) 320, (b) 3 × 320, (c) 6 × 160 nm and (d) cross sectional SEM image of the 6 × 160 nm film.

The scanning electron microscopy (SEM) surface images confirm the polycrystalline nature and the dense crystalline grains, as shown in Fig. 2 (a-c) corresponding to film thicknesses of 320, 3 × 320 and 6 × 160 nm, respectively. Fig. 2d shows a cross-sectional SEM image of the 6 × 160 nm film. This image depicts a columnar growth of the film and the presence of an interlayer between the film and substrate. The surface becomes rougher with increasing thickness, which is associated with a gradual formation of nano-grains on the surface (Fig. 2d).

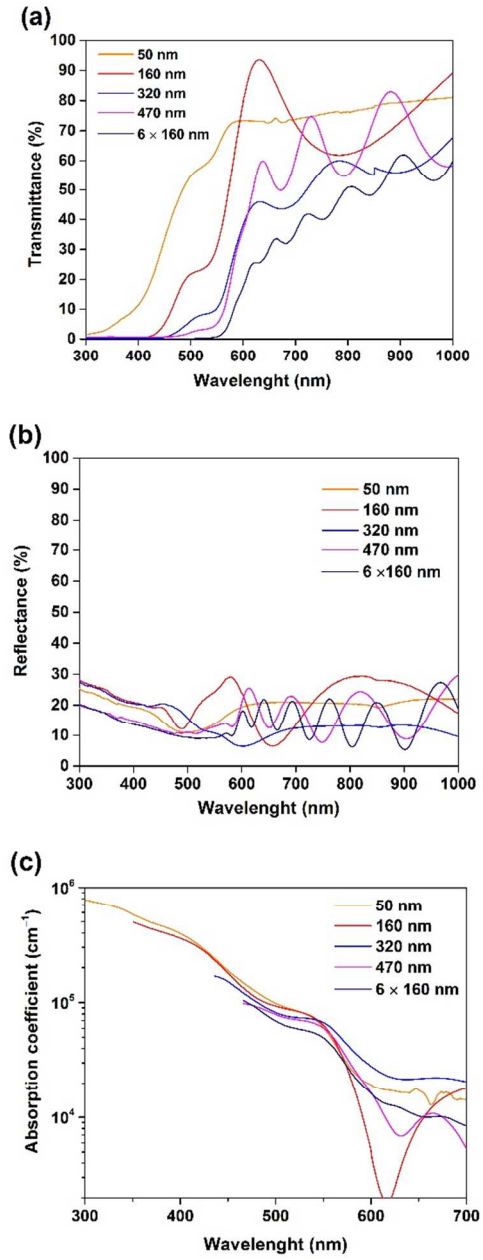

Fig. 3 The (a) transmittance, (b) reflectance, (c) absorbance and (d) absorption coefficient spectra of Ta_3N_5 films with different thicknesses.

The transmittance spectra of the films deposited on fused glass are shown in Fig. 3a. A continuous shift of the transmittance towards higher wavelengths was observed with increasing film thickness, as expected from the Beer-Lambert law. The spectra also show typical fringes resulting from interferences between the air/film and film/substrate interfaces. In the reflectance spectra (Fig. 3b), an average reflectance of approximately 20% beyond 400 nm and an increase of approximately 30% for lower wavelengths were observed. To

accurately acquire the absorption coefficient of the samples, non-

Table 1. Electrical and transport properties of Ta_3N_5 films at different thickness.

Ta_3N_5 thickness (nm)	Resistivity (Ω cm)	Charge carrier concentration (cm^{-3})	Mobility ($cm^2 V^{-1} s^{-1}$)	Carrier lifetime (ps)
160	32	1.0×10^{17}	1.9	5.0
320	0.02	2.6×10^{20}	1.8	4.0
470	0.01	5.1×10^{20}	1.3	3.1
3 × 320	58	2.4×10^{16}	4.4	7.3
6 × 160	0.45	4.7×10^{18}	2.9	8.7
$BiVO_4$ [38]	5.68	2.5×10^{19}	0.044	40000
α-Fe_2O_3 [39,40]	2.80	1.5×10^{16}	1.48	3

saturated parts of the transmission spectrum was used, as seen in Fig. 3c. An absorbance edge of ~600 nm was observed for all of the films, which is consistent with the reported 2.1 eV band-gap of Ta_3N_5.[17,20,23,30] The absorption coefficient appears to monotonically decrease with increasing wavelengths, and the values are relatively low, starting from 8×10^5 to 1×10^4 cm^{-1} in the spectral range relevant to the PEC measurement (300 to 600 nm). Two broad absorbance peaks at ~430 and ~540 nm precisely reflect the density of state of the electronic structure obtained by advanced density functional theory calculation.[30] Although Dabirian et al. attributed this absorbance to the resonance of Ta_3N_5 films with conductive platinum under the nitride films,[31] the absorption more likely originates from the direct/indirect band-gap transition of Ta_3N_5, as reported by Pinaud et al.[32]

The dielectric constant is an important parameter that describes the interaction of the electric field with the material medium. For instance, the carrier concentration can be calculated, which is a significant value that is relevant to the PEC performance. The dielectric constant of Ta_3N_5 in a powder system equal to 110 was used to calculate the carrier concentration in the literature.[25] However, the dielectric constant is often overestimated when the powder semiconductor is used for the measurement due to extrinsic microstructural features, such as twin boundaries or the presence of a barrier-layer capacitor effect.[33] Thin films are in the form of more compact structure with less extrinsic effects. In this work, we estimated the dielectric constant using the complex index of refraction $N = n + ik$. From the fringes observed in the transmittance and reflectance spectra (Fig. 3a), we can deduce the following simplified equation for the refractive index n and, from the absorption coefficient, the absorption index k (or absorptance);[34]

$$n = \frac{f(\lambda_1 \lambda_2)}{2(\lambda_1 - \lambda_2)t}$$

where f is the fringe number, λ_1 is the maximum wavelength, λ_2 is the minimum wavelength and t is the film thickness.

The absorption index is equal to $k = \frac{\alpha\lambda}{4\pi}$, where α is the absorption coefficient. In the spectral range of 600-900 nm, we can calculate n = 4.2 and k = 0.06. Correlating the complex index to the dielectric properties then becomes:

$$\varepsilon = \varepsilon_1 + i\varepsilon_2 = N^2 = (n + ik)^2$$

We can deduce the dielectric constant $\varepsilon_1 = n^2 - k^2 \approx n^2$ (for low absorption) and dielectric losses $\varepsilon_2 = 2nk$. Thus, the obtained dielectric constant was 17 with tangent losses (= $\varepsilon_2/\varepsilon_1$) at approximately 0.03 in the visible spectral range from 10^{14} to 10^{15} Hz. Usually, dielectric constant is dependent on the frequency; the dielectric constant increases with decreasing frequency. For other measurements, such as microwave and capacitance measurements, using lower frequencies may lead to higher dielectric constants.

The thin films were tested for their electrochemical properties. First, the conducted capacitive current was measured by varying the scan rates in cyclic voltammetry (CV; Fig. S1, Table S1). Generally, the capacitive current increases in both reduction and oxidation at more negative potentials, which may result from extra surface redox species that appear only at these potentials. This behavior was also observed for all of the Ta_3N_5 films with different thicknesses, suggesting that it is intrinsic for the Ta_3N_5 films. The fact that capacitive current increased with increasing film thickness (Fig. S2) indicates an increase of the relative surface area by 9-fold for the 6 × 160 nm film relative to the 160 nm film (Table S1).

To undergo a photocatalytic/photoelectrochemical reaction, a semiconductor photocatalyst must possess suitable band positions (conduction band and valence band) with respect to the water redox potentials (thermodynamic requirement).[5,7] To estimate band positions, Mott-Schottky plots using impedance spectroscopy were obtained in an attempt to retrieve the flat-band potential. Fig. S3 shows the Mott-Schottky plots for the Ta_3N_5 films with different thicknesses, based on the impedance data shown in Figs. S4 and S5. All of the Ta_3N_5 films exhibited positive slopes, which are characteristic of n-type semiconductors. The selection of a suitable potential window for extrapolation from the Mott-Schottky plots is crucial to accurately obtain the flat-band potentials. For this purpose, the Faradaic current should remain negligible. However, the non-flat behavior of the capacitive current as observed in Fig. S1 causes difficulty in selecting the right potential window for flat

band potential measurement. At the potential range from −1.2 to +1.0 V vs. RHE, the Mott-Schottky analysis leads to a flat-band potential from −0.1 to 0 V vs. RHE, which is consistent with reported values.[18,25] Using a different potential range at more positive potentials, the flat-band potential can be found between +0.8 and +1.1 V vs. RHE. These results show much more positive flat-band potential compared with those reported. Notably, the flat-band potentials mentioned in the literature were taken at different potential ranges, resulting in different flat-band potentials. Ideally, the Mott-Schottky analysis is suitable for a single-crystal material with moderate doping content and a good ohmic contact,[35] which is not the case for these samples nor those reported in the literature.[18,25] Additionally, the flat-band potential should not depend on the frequency used. However, as seen in Fig. S3, there is slight difference in the flat-band potential with different frequencies (250-1000 Hz), which might arise from the surface state capacitance and associated double-layer capacitance at the semiconductor-electrolyte interface, as also observed in the CV at high scan rates (Fig. S1).[35] Further detailed investigation is essential to fully understand the issues mentioned above.

Using a dielectric constant of 17, the charge carrier concentration can be calculated from the slopes in the Mott-Schottky plots (Fig. S3), and the results are listed in Table S2. Using a geometric area of the films, the obtained values were ~4 × 10^{20} cm^{-3} for the 160, 320, and 470 nm films and 2 × 10^{21} cm^{-3} for the 6 × 160 nm film. If the relative surface area (Table S1) of the stacked film (6 × 160 nm) was used, the carrier concentration of this film was in the same range as the rest of the samples. Clearly, the donor density measurement from the Mott-Schottky analysis is very complex; therefore, the carrier concentrations of the films were also measured using Hall measurements.

In Table 1, we report the electronic transport properties (carrier mobility) and spectroscopic measurements (carrier recombination). These two parameters determine the diffusion length of the material and can be correlated to the PEC performances. Van der Pauw four-probe measurement provides the resistivity of the material, and the Hall measurements provide the charge carrier concentration. As seen in Table 1, the resistivity of the films decreased from 32 to 0.01 Ω cm with a thickness increase from 160 to 470 nm, which correlates to the crystallinity of the films. For the stacked films (3 × 320 nm and 6 × 160 nm), the resistivity increased to 55 and 0.45 Ω cm, respectively. The stacking growth of the Ta_3N_5 material is considered to cause additional resistivity especially at the interfaces. However, all of these values are within the range of typical semiconductor materials (10^{-3}-10^{3} Ω cm). The carrier concentrations are in the range of 10^{16} to 10^{20} cm^{-3}, which are within the same range for the other reported photoanodes, such as hematite α-Fe_2O_3,[38] or bismuth vanadate $BiVO_4$.[39,40] The calculated mobilities were in the range of 1.3 to 4.4 cm^2 V^{-1} s^{-1}. Thicker films was found to possess higher mobility.

Because femtosecond (fs) transient absorption spectroscopy provides direct information regarding the carrier dynamics and excited-state deactivation pathways, including carrier trapping, we utilized this method to probe the events that occurred due to photoexcitation of the Ta_3N_5 films with different thickness. The fs transient absorption spectroscopy employed a white-light-continuum probe pulse generated in a 2-mm-thick sapphire plate in an Ultrafast System LLC spectrometer. A pulse energy of a few μJ of the fundamental output of a Ti:sapphire fs regenerative amplifier operating at 800 nm with 35 fs pulses and a repetition rate of 1 kHz was used. Pump pulses at 440 nm were created from fs pulses generated in an optical parametric amplifier (Spectra-Physics). The pump and probe beams were focused on the sample solution, and the transmitted probe light through the

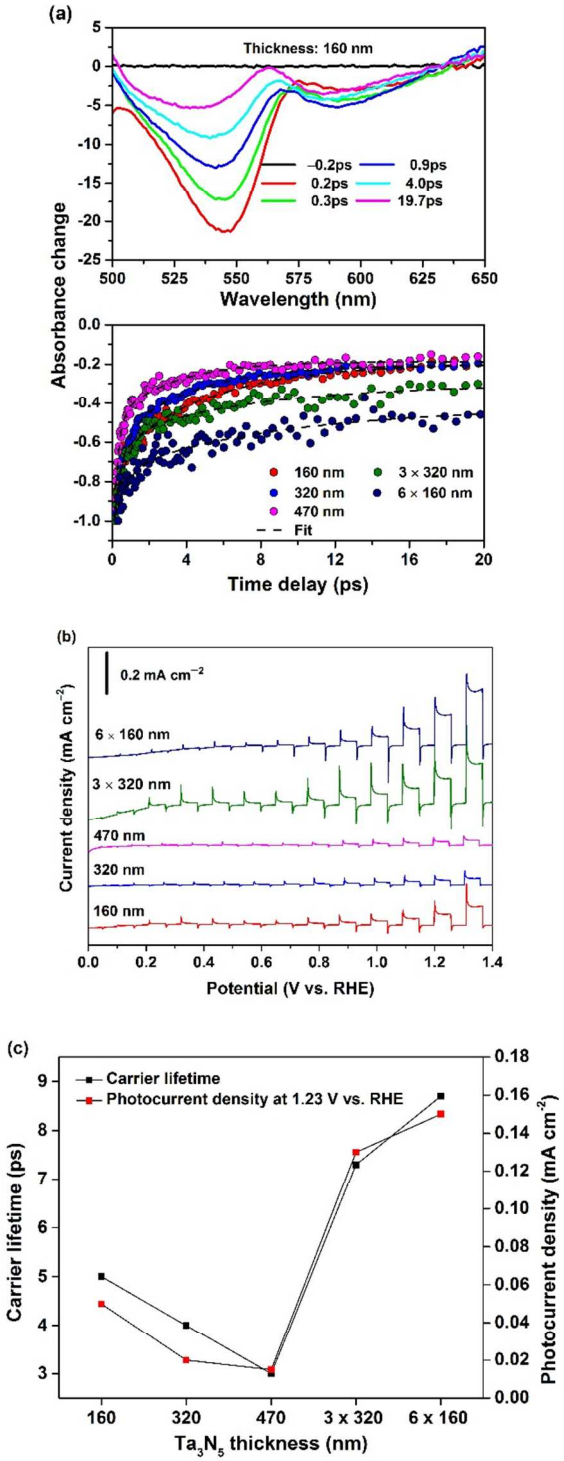

Fig. 4 (a) The transient absorption spectra at different time delay (top panel), and the kinetics of the ground state bleach recovery after 480 nm optical excitation (lower panel), (b) The

LSVs for different Ta_3N_5 films thicknesses and (c) the variation of the carrier lifetime and photocurrent density with different thicknesses of Ta_3N_5 films.

samples was collected and focused on the broadband UV-visible detector to record the time-resolved transient absorption spectra. The intrinsic defects in Ta_3N_5 can significantly reduce the carrier lifetime and consequently decrease the photocurrent. It is well known that the carrier lifetime is significantly elongated by the film morphology, grain size and crystallinity. Here, we explore the carrier dynamics of the Ta_3N_5 thin films using broadband transient absorption spectroscopy with 120 fs temporal resolution. As can be clearly seen in Fig. 4a, the carrier recombination decreased as reflected from the ground state bleach recovery for the thin films (160, 320 and 470 nm) under the same experimental conditions. It is known that a decrease in film thickness leads to a good electrons-hole transport because the photogenerated carriers have short distance to travel with less chance of being trapped by surface defects.[27] However, for multiply deposited thicker films (3 × 320 nm and 6 × 160 nm), we can note a modest increase in the carrier lifetime compared with the thinner films. The ground-state bleach recovery of Ta_3N_5 due to carrier recombination becomes slower as the thickness of the film increases. The observed dynamics can be attributed to the decrease in carrier trapping, indicating that there are less defects in the thicker film compared with the thinner one. This observation is consistent with XRD patterns (Fig. 1) and SEM images (Fig. 2) which indicate more crystalline with the thicker films. The measured lifetimes were in the range of 3.1 to 8.7 ps (Table 1), consistent with the low lifetime of 12 ps reported on Ta_3N_5 powder.[36]

For investigation of the photoelectrochemical (PEC) properties, current-potential curves were obtained from linear sweep voltammetry (LSV) from 0 to +1.4 V vs. reversible hydrogen electrode (RHE) at a scan rate of 10 mV s^{-1} in an aqueous Na_2SO_4 solution (pH 13) under intermittent irradiation using a solar simulator, AM 1.5G, as shown in Fig. 4b. For all of the films, an anodic photocurrent was observed at +0.5 V vs. RHE. For the thinner films (160 to 470 nm), the best PEC performance was observed for the 160 nm film. The photocurrent decreased as the film thickness increased although the absorbance of the film increased, indicating better electronic transport in thinner films. A higher photocurrent was observed for the thick films that were made by stacking multiple depositions (3 × 320 and 6 × 160 nm) compared with those for the thin films. This stacking procedure for deposition may lead to an increase in the porosity of the material after annealing treatment, as evidenced by higher capacitance (Table S1). It was reported that the PEC performance in such porous structure was better than that in the dense thick films.[37] Porosity may affect various properties of the semiconductors, such as surface area and resultant transport properties, which may in turn improve the PEC performance. In the next session, we will try to rationalize the measured properties with the obtained PEC performance.

The PEC performance was compared with the measured values for the photophysical properties. The relative surface area (9-fold difference; Table S1), the absorbance (Fig. 3, monotonic increase with thickness), or the mobility (Table 1) cannot alone explain the PEC performance. In contrast, the carrier recombination (Table 1) adequately fits the behavior when the photocurrent is +1.23 V vs. RHE, as depicted in Fig. 4c. This result may indicate that the PEC performance of the Ta_3N_5 films is essentially reflected by the carrier lifetime. The measured carrier lifetimes for the Ta_3N_5 films were found to be very low compared with, e.g., $BiVO_4$, which was 10^4 larger.[33] High PEC performance of $BiVO_4$ was achieved, despite a very low mobility (approximately 0.044 cm^2 V^{-1} s^{-1}), due to its high carrier lifetime (approximately 40 ns).[38] One particular obstacle in the use of a Ta_3N_5 film as a photoanode is its high onset potential for water oxidation (approximately +0.6 vs. RHE or higher) despite the fact that its flat-band potential is reported to be approximately −0.05 to −0.1 V vs. RHE.[20,22,24,25,27] Here, we suggest the low carrier lifetime as an intrinsic kinetic barrier that causes the large onset potentials and then limit the overall PEC performance. This result may be a key finding because it illustrates the intrinsic limitation of the Ta_3N_5 electronic structure for use as the photoanode for water splitting. Extremely fast carrier recombinations together with low carrier mobilities are the major concern in the development of Ta_3N_5 as an efficient photocatalyst.

The stability of the photoanode is a very important criterion for PEC reaction. Photocatalyst surface modification with cocatalyst is a conventional way to increase the stability.[5] The addition of cobalt or a cobalt system, have been reported to tremendously improve the PEC performance.[20-25] Therefore, the Ta_3N_5 films were decorated with 10 nm of DC-sputtered cobalt. Their photoelectrochemical performance is depicted in Fig. S6. The photocurrent density on the films with Co cocatalyst is approximately 6 times higher than on the unmodified film at +1.23 V vs. RHE. This increased anodic photocurrent was also observed for the other films prepared in this study upon modification with a Co species. The modification of Co leads to improved charge separation, created a new interface between the Ta_3N_5 and the Co species, and improved the catalytic function of the photoanode surface. In addition, the stability of the film (Fig. 5) shows that the anodic photocurrent was very stable over time. The surface of the film was protected against the electrolyte corrosion when it was completely covered by 10 nm of Co, which leads to an efficient charge transfer and increases the reaction rate.[13]

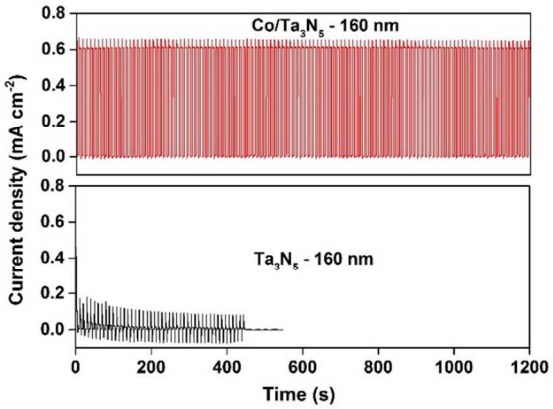

Fig. 5 Chronoamperometry at 1.23 V vs. RHE of Ta_3N_5 with and without Co at 160 nm thickness under AM1.5G solar light irradiation in a 0.1 M Na_2SO_4 electrolyte solution.

Interestingly, the photocatalytic hydrogen evolution performance from a methanol-containing solution remains relatively low on Pt-decorated Ta_3N_5 powders, despite their reported suitable band positions.[41-43] Our recent paper noted that the hydrogen evolution is highly affected by the surface states present on the topmost layer of Ta_3N_5.[41] In attempt to understand this behavior, a 160 nm Ta_3N_5 film was deposited on 200 nm platinum that was grown on a (100) silicon substrate. The PEC performance of the corresponding film is presented in Fig. S7. Interestingly, a cathodic photocurrent, a signature of p-type semiconductors, was observed. This result suggests that a new metal/semiconductor interface, depending on their identities, drastically affects the electronic structure, even altering the n- or p-type nature of the semiconductor. Further investigation is ongoing to better understand this behavior of the Ta_3N_5/Pt electrode. This finding illustrates the complex character of Ta_3N_5, and further analyses are needed to elucidate the nature of this material.

Conclusions

In this study, Ta_3N_5 films with different thicknesses were synthesized by DC sputtering combined with nitridation and were characterized to accurately determine their (photo)physical properties, such as the absorption coefficient, carrier mobility, carrier lifetime, relative surface area, and PEC performance. For all the Ta_3N_5 samples prepared with various thickness, low carrier lifetime was measured (<10 ps). This low value of carrier dynamics may play as an intrinsic kinetic barrier of Ta_3N_5 for PEC application, which may explain high onset potentials required for water oxidation (>0.6 V vs. RHE) reported in the literature for Ta_3N_5. The PEC performance of the bare Ta_3N_5 was strongly reflected by the carrier recombination dynamics. Because one gear deficiency can cause the limited overall deficiency in the PEC mechanism, this study provides a good pedagogic example to provide the measure of improvement based on the global characterization of the photoelectrode, including the absorption coefficient, charge separation, charge diffusion and electron-hole reactions with the electrolyte. Construction of new interface with, e.g., cocatalyst and back contact was suggested to tremendously affect PEC nature (p or n), activity and stability, and thus needs to be elucidated for the improved PEC performance.

Experimental

Material Synthesis

Ta_3N_5 thin films were grown using direct current (DC) magnetron reactive sputtering with a pure tantalum (Ta) target. Deposition was performed on Ta foil and fused glass (FG) substrates at room temperature. The tantalum nitride phase was obtained by the addition of reactive nitrogen (N_2) gas to the argon (Ar) sputtering gas. The Ar and N_2 flows were fixed at 4 and 10 standard cubic centimeters per minute (sccm), respectively. The total pressure and DC power density to target were fixed at 0.8 Pa and 7.3 W cm^{-2}, respectively. Post-annealing treatments were conducted for 3 h at 550°C under air for the oxidation phase and for 3 h under 200 mL min^{-1} continuous ammonia (NH_3) flow at 900°C for the nitridation phase. Thin film thicknesses were measured using a profilometer on a glass substrate masked with a small piece of silicon.

Structural characterization

The structural characterization of the thin films was performed by recording conventional θ-2θ X-ray diffraction patterns from a Bruker Discover diffractometer (Cu $K\alpha_1$ radiation) with a 0.01° step size and a 0.5 s counting time per step.

Optical characterization

The UV-visible transmittances and reflectances were obtained on films deposited on FG substrates. The spectra were recorded in the range of 200 to 1000 nm using a JASCO V-670 spectrophotometer. For each sample, the absorbance was extracted by accounting for the transmittance and the reflectance contributions:

$$A = I - (T + R)$$

where A is absorbance, I is incident light, T is transmittance, and R is reflectance.[35]

The absorption coefficient was calculated using the equation:

$$\alpha = \frac{1}{t} \ln\left(\frac{1-R}{T}\right)$$

where α is absorption coefficient, t is thickness, T is transmittance, and R is reflectance.[44]

Transport measurements

The electrical transport measurements were performed in a physical properties measurement system (PPMS) from Quantum Design. The resistivity, carrier charge density and mobility were characterized using four probes. Van der Pauw and Hall effect measurements were obtained at room temperature.[45]

Electrochemical and photoelectrochemical characterization

Electrochemical impedance spectroscopy was performed to estimate the flat-band potential and the band positions of the

prepared Ta_3N_5 films. The fabricated Ta_3N_5 film, a platinum electrode, and a Ag/AgCl (saturated in KCl aq.) electrode were used as the working, counter and reference electrodes, respectively. The electrolyte used for the electrochemical impedance spectroscopic investigations was a 0.5 M NaOH solution (pH = 13.5). The measurements were performed using a 16-channel research-grade potentiostat system (VMP3) from BioLogic Science Instruments in a conventional three-electrode single electrochemical cell. To determine the potential window for the Mott-Schottky analysis, cyclic voltammetry experiments were conducted under bubbling Ar with various scan rates of 10 - 500 mV s^{-1} scan rate between 0 to 1.23 V vs. RHE. The relative surface area of the films were calculated based on capacitive current measured at different scan rates.[27]

Impedance spectra were recorded between 10 Hz to 200 kHz under bubbling Ar, and the amplitude of the superimposed sinusoidal potential signal was 5 mV for each of the 70 steps in the potential window starting from 1.5 to 0 V vs. RHE under dark conditions. The Mott-Schottky plots only depict the potential window in which the faradic current remains negligible in accordance with the cyclic voltammetry. The flat band potential of the films were obtained by extrapolation to the X-axis of the Mott-Schottky (C^{-2} against potential) and the majority charge carrier concentration (N_A) can be extracted can be obtained from the slope of the linear fit according to the following equation.[46-48]

$$\frac{1}{C^2} = \frac{2}{A^2 e \varepsilon \varepsilon_o N_A}\left(E - E_{FB} - \frac{k_B T}{e}\right)$$

where C is interfacial capacitance and E is the applied potential. Here, the constant A is the area, ε is the dielectric constant of the semiconductor, ε_0 is the permittivity of free space, T is the absolute temperature, e is the electronic charge and k_B is the Boltzmann's constant.

Photoelectrochemical measurements were conducted using 3-electrode system and a potentiostat (Biologic, VMP3). The Ta_3N_5 electrode was used as the working electrode, the Ag/AgCl electrode (saturated in KCl aq.) was used as the reference electrode, and a platinum wire was used as the counter electrode. The electrolyte used was 0.1 M Na_2SO_4 aq. at an adjusted pH of 13 by the addition of NaOH. A solar simulator (Peccell Technologies, PEC-L15) was used to illuminate AM 1.5 G mimicking spectra. An anodic sweep was conducted at 10 mV s^{-1}.

Acknowledgements

This reported work is supported by King Abdullah University of Science and Technology (KAUST).

Notes and references

[a] *Division of Physical Sciences and Engineering,*
KAUST Catalysis Center (KCC),
King Abdullah University of Science and Technology (KAUST)
Thuwal, 23955-6900 (Saudi Arabia)
*E-mail: kazuhiro.takanabe@kaust.edu.sa
[b] *Solar and Photovoltaic Engineering Research Center,*
King Abdullah University of Science and Technology (KAUST)
Thuwal, 23955-6900 (Saudi Arabia)

† Electronic Supplementary Information (ESI) available: [Additional experimental data, Figs. S1-S7, Tables S1 and S2.]. See DOI: 10.1039/b000000x/

1 A. Bard, and M.A. Fox, *Acc. Chem. Res.*, 1995, **28**, 141.
2 O. Khaselev, and J. Turner, *Science*, 1998, **280**, 425.
3 M. Grätzel, *Nature*, 2001, **414**, 338.
4 M. Walter, E. Warren, J. McKone, S. Boettcher, Q. Mi, E. Santori, and N. Lewis, *Chem. Rev.,* 2010, **110**, 11, 6473.
5 K. Takanabe, and K. Domen, *Green*, 2011, **1**, 313.
6 D. Nocera, *Acc. Chem. Res*., 2012, **45**, 5, 767.
7 K. Takanabe, and K. Domen, *ChemCatChem*, 2012, **4**, 1485.
8 A. Fujishima, and K. Honda, *Nature,* 1972, **238.**
9 K. Sivula, F. Le Formal, and M. Gratzel, *ChemSusChem*, 2011, **4**, 432.
10 F. Abdi, L. Han, A. Smets, M. Zeman, B. Dam, and R. van de Krol, *Nature Commun*., 2013, **4**, 2195.
11 T.W. Kim, and K-S. Choi, *Science*, 2014, **343**, 990.
12 I. Fujimoto, N. Wang, R. Saito, Y. Miseki, T. Gunji, K. Sayama, *Int. J. Hydrogen Energy*, 2014, **39**, 2454.
13 M. Higashi, K. Domen, and R. Abe, *J. Am. Chem. Soc.*, 2012, **134**, 6968.
14 J. Kubota, and K. Domen, *Electrochem. Soc. Interface Summer* 2013.
15 K. Maeda, and K. Domen, *J. Phys. Chem. C*, 2007, **111**, 7851.
16 W.-J. Chun, A. Ishikawa, H. Fujisawa, T. Takata, J.N. Kondo, M. Hara, M. Kawai, Y. Matsumoto, and K. Domen, *J. Phys. Chem. B,* 2003, **107**, 1798.
17 M. Hara, G. Hitoki, T. Takata, J.N. Kondo, H. Kobayashi, and K. Domen, *Catal. Today*, 2003, **78**, 555.
18 H. Dang, N. Hahn, H. Park, A. Bard, and B. Mullins, *J. Phys. Chem. C*, 2012, **116**, 19225.
19 M. Li, W. Luo, D. Cao, X. Zhao, Z. Li, T. Yu, and Z. Zou, *Angew. Chem. Int. Ed*., 2013, **52**, 11016.
20 Y. Li, T. Takata, D. Cha, K. Takanabe, T. Minegishi, J. Kubota and K. Domen, *Adv. Mater.*, 2013, **25**, 125.
21 R. Gao, L. Hu, M. Chen, and L. Wu, *Small*, 2014, **10**, 15, 3038.
22 G. Liu, J. Shi, F. Zhang, Z, Chen, J. Han, C. Ding, S. Chen, Z. Wang, H. Han and C. Li, *Angew. Chem. Int. Ed.*, 2014, **53**, 7295.
23 M. Hara, E. Chiba, A. Ishikawa, T. Takata, J.N. Kondo and. K. Domen. *J. Phys. Chem. B*, 2003, **107**, 13441.
24 Y. Cong, H. S. Park, S.Wang, H.X. Dang, F.-R.F. Fan, C. B. Mullins, *J. Phys. Chem. C*, 2012, **116**, 14541.
25 Y. Li, L. Zhang, A. Torres-Pardo, J. M. González-Calbet, Y. Ma, P. Oleynikov, O. Terasaki, S. Asahina, M. Shima, D. Cha, L. Zhao, K. Takanabe, J. Kubota, K. Domen, *Nature Commun*., 2013, **4**, 2566.
26 A. Ishikawa, T. Takata, J. N. Kondo, M. Hara, K. Domen, *J. Phys. Chem. B*, 2004, **108**, 11049.
27 B.A. Pinaud, P.C.K. Vesborg, and T.F. Jaramillo, *J. Phys. Chem. C*, 2012, **116**, 15918.
28 X. Feng, T. LaTempa, J. Basham, G. Mor, O. Varghese and C. Grimes, *Nano Lett*., 2010, **10**, 948.
29 D. Yokoyama, H. Hashiguchi, K. Maeda, T. Minegishi, T. Takata, R. Abe, J. Kubota, K. Domen, *Thin Solid Films*, 2011, **519**, 2087.
30 M. Harb, P. Sautet, E. Nurlaela, P. Raybaud, L. Cavallo, K. Domen, J-M. Basset, and K. Takanabe, *Phys. Chem. Chem. Phys*., 2014, 16, 20548.
31 A. Dabirian and R. van de Krol, *Appl. Phys. Lett*., 2013, **102**, 033905.
32 B.A. Pinaud, A. Vailionis and T. F. Jaramillo, *Chem. Mater*., 2014, **26**, 1576.

33 Y-I. Kim, W. Si, P. Woodward, E. Sutter, S. Park, and T. Vogt, *Chem. Mater*., 2007, **19**, 618.
34 R. Swanepoel, *J. Phys. E: Sci. Instrum.,* 1983, **16,** 1214.
35 Z. Chen, T.F. Jaramillo, T.G. Deutsch, A. Kleiman-Shwarsctein, A.J. Forman, N. Gaillard, R. Garland, K. Takanabe, C. Heske, M. Sunkara, E.W. McFarland, K. Domen, E.L. Miller, J.A. Turner, and H.N. Dinh, *J. Mater. Res*., 2010, **25**, 3-16.
36 A. Furube, K. Maeda, and K. Domen, *Proc. of SPIE*, 2011, **8109,** 810904.
37 B.A. Pinaud, P.C. Vesborg, T.F. Jaramillo, *J. Phys. Chem. C*, 2012, **116**, 15918
38 F. Abdi, T. Savenije, M. May, B. Dam, and R. van de Krol, *J. Phys. Chem. Lett*., 2013, **4**, 2752.
39 A. Joly, J. Williams, S. Chambers, G. Xiong, W. Hess, and D. Laman, *J. Appl. Phys*., 2006, **99**, 05352.
40 S. Shinde, R. Bansode, C. Bhosale, and K. Rajpure, *J. Semicond*., 2011, **32**, 1.
41 E. Nurlaela, S. Ould-Chikh, M. Harb, S. del Gobbo , M. Aouine, E. Puzenat, P.Sautet, K. Domen, J-M. Basset, and K. Takanabe, *Chem. Mater*., 2014, **26**, 4812.
42 Y. Fukasawa, K. Takanabe, A. Shimojima, M. Antonietti, K. Domen, and T. Okubo, *Chem. Asian J*., 2011, **6**, 103.
43 X. Liu, L. Zhao, K. Domen, and K. Takanabe, *Mater. Res. Bull*., 2014, **49**, 58.
44 J. F. Muth, J. H. Lee, I. K. Shmagin, R. M. Kolbas, H. C. Casey Jr., B. P. Keller, U. K. Mishra, and S. P. DenBaars, *Appl. Phys. Lett.*, 1997, **71**, 2572.
45 L.J. van der Pauw, *Res. Repts*., 1958, **13**, 1.
46 V. A. Myamlin and Yu V. Pleskov, *Electrochemistry of Semiconductors*, 1967, New York: Plenum.
47 N. F. Mott, *Proc. R. Soc. A*, 1939, **171**, 27.
48 W. Schottky, *Z. Phys*., 1939, **113**, 367.

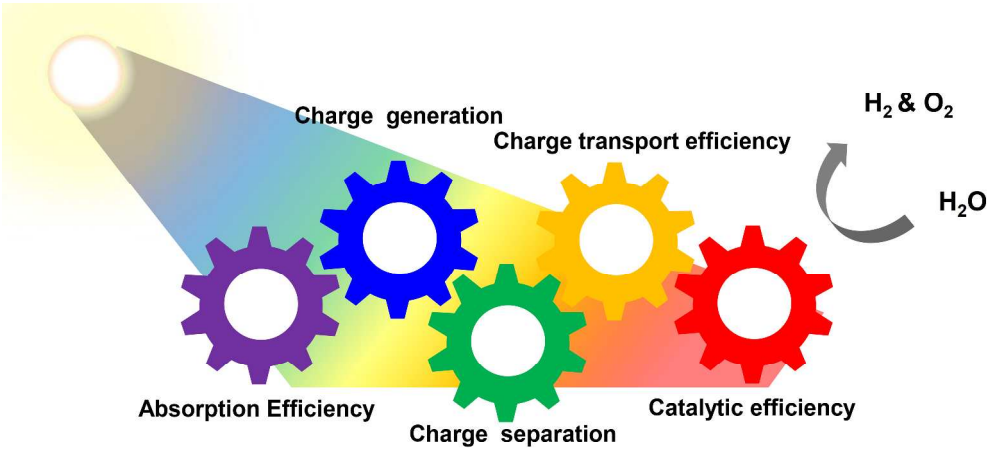

1977x892mm (72 x 72 DPI)